SCIENCE CHINA
Information Sciences

August 2023, Vol. 66 180503:1–180503:7
https://doi.org/10.1007/s11432-022-3641-x

• RESEARCH PAPER •
Special Topic: Quantum Infomation

Low-loss, dual-polarization asymmetric Mach-Zehnder interferometer chips for quantum key distribution

Meizhen REN*, Lai ZHOU & Zhiliang YUAN

Beijing Academy of Quantum Information Sciences, Beijing 100193*, China*

Received 28 July 2022/Revised 9 October 2022/Accepted 6 December 2022/Published online 19 June 2023

Abstract We have developed the first low-loss, dual-polarization, asymmetric Mach-Zehnder interferometer (AMZI) chip for phase-coding quantum key distribution (QKD) using silica planar lightwave circuit technology. The transmitter and receiver modules have a polarization extinction ratio greater than 20 and 15 dB, respectively. Using a birefringent Mach-Zehnder interferometer, a polarization beam splitter is integrated into the receiver chip, while the polarization rotation function is obtained via a half-wave plate thin film. The receiver chip is entirely passive and has an excellent fiber C fiber loss of 1.90 dB, while the transmitter's AMZI contains thermo-optical electrodes for adjusting the output pulses' relative phase and intensity ratio. The chips are evaluated to have an interference visibility of greater than 98% across a broad temperature range, demonstrating their suitability for quantum key distribution applications.

Keywords quantum key distribution, dual-polarization, asymmetric Mach-Zehnder interferometer, polarization beam splitter, silica-based planar lightwave circuit technology

Citation Ren M Z, Zhou L, Yuan Z L. Low-loss, dual-polarization asymmetric Mach-Zehnder interferometer chips for quantum key distribution. Sci China Inf Sci, 2023, 66(8): 180503, https://doi.org/10.1007/s11432-022-3641-x

1 Introduction

Quantum key distribution (QKD) is an attractive, quantum-resistant method for distributing encryption keys between remote parties, the secrecy of which is independent of the computing power of an adversary. Since the first experiment over a 32-cm air gap [1], continuous efforts have been made to make the technology practical, including extending the communication distance and the secure key rate (SKR) [2]. Due to its low transmission loss at telecom wavelengths and extensive network infrastructure availability, fiber is the most common communication medium. Fiber-based QKD systems have been shown to deliver a continuous rate greater than 10 Mbit/s over short distances [2], which is sufficient for many applications, such as securing high-definition video links or data transmission of the human genome. Furthermore, the communication distance for prepare-and-measure systems with ultralow noise detectors has been increased to 420 km [3], whereas twin-field QKD can be used over much greater distances. While twin-field QKD can provide higher rates for long-haul links [4, 5], standard decoy-state BB84 QKD remains the most practical option for links less than 200 km.

Integrated photonics is currently being utilized to increase the practicality of QKD [6, 7]. Substituting bulky and costly optics with compact devices [8] would ensure scalability, manufacturability, and stability and therefore has the potential to stimulate a broader deployment of QKD technology. Several material platforms have been explored with considerable success to develop compact and versatile QKD chips [9]. Indium phosphide (InP) [7, 10, 11] chips permit monolithic integration of light sources and high-speed modulators, whereas silicon photonics [6, 12, 13] profit from the well-established complementary metal-oxide-semiconductor integration.

However, chips fabricated from these materials suffer from significant propagation and/or coupling loss, making them unsuitable for integrating delay lines and quantum receivers (QRx). Silicon nitride [6, 9]

* Corresponding author (email: renmeizhen@semi.ac.cn)

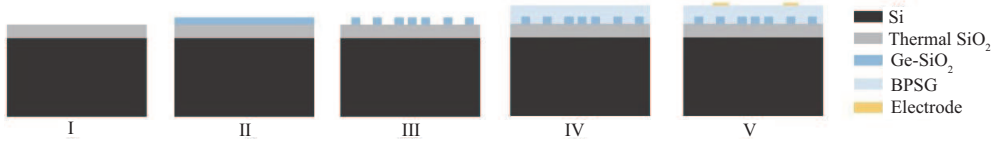

Figure 1 (Color online) Fabrication flow of the silica-based PLC technology.

and silica-on-silicon photonics [14–16] can provide low-loss circuits, with transmission losses of 0.5 and 0.03 dB/cm, respectively. In addition, the coupling loss between a silica-on-silicon waveguide and a fiber is extremely low, less than 0.4 dB/end, because the waveguide is composed of the same material as the fiber. Since the loss of a QRx directly impacts its overall performance, it is essential to have a QRx with low losses to achieve a higher SKR and longer transmission distance. The silica planar lightwave circuit (PLC) platform stands out among various integrated platforms thanks to its low transmission and fiber coupling loss.

Because such qubits can transmit over great distances with minimal decoherence, time-bin phase encoding is a viable option for fiber-optic QKD systems. Here, asymmetric Mach-Zehnder interferometers (AMZIs) are employed for qubit preparation and measurement. A photon can pass through four equally probable paths without deterministic routing: short-short, short-long, long-short, and long-long arms of the two AMZIs. Photons that pass through both short (long) arms without interference are effectively lost. Polarization routing can force a photon to take only short C long and long C short paths [2, 17, 18] and achieve a 3 dB routing advantage as a result.

Several groups have utilized low-loss photonic integration platforms to develop AMZI [14, 15] or asymmetric Michaelson interferometers [16] for QKD applications in recent years. However, despite their routing advantage, no effort has yet been made to develop dual-polarization AMZI chips. In this paper, we fabricate the first dual-polarization AMZI structure suitable for high SKR QKD systems using a silica-based PLC platform.

2 Device fabrication

The devices described in this paper were fabricated using silica-based PLC technology. The manufacturing process is depicted in Figure 1. This technology consists of thermal oxidation, plasma-enhanced chemical vapor deposition (PECVD), photolithography, inductively coupled plasma (ICP) etching, borophosphosilicate glass (BPSG) overcladding deposition, magnetron sputtering, evaporating, and liftoff technology. First, thermal oxidation at 1050°C is used to fabricate a 20 μm thick SiO_2 down cladding, then PECVD is used to create a 6 μm thick GeO_2-SiO_2 core, and finally, a 1 μm thick poly-Si hard mask layer was grown by low-pressure chemical vapor deposition. Next, photolithography and ICP etching are utilized to complete the pattern transfer. Then, PECVD is used to form an upper BPSG cladding of 20 μm thickness. Finally, thin-film Ti-W heating electrodes are fabricated using photolithography, magnetron sputtering, and liftoff, while Pt-Au leading electrodes are fabricated using photolithography, evaporating, and liftoff. The wafer was then sliced, and the chip's waveguide end faces were polished.

3 Polarization beam splitter and polarization rotator

Two essential components for the dual-polarization phase-coding scheme are the polarization beam splitter (PBS) and the polarization rotator (PR) (or polarization splitter-rotator, PSR). While PSR can be easily implemented on a silicon-on-insulator (SOI) or InP platform [19, 20], the associated losses of 1.25 dB/cm for SOI waveguide [12] and 3 dB/cm for InP waveguide [7, 10] are unacceptable for use in a QKD receiver.

We implement the required PBS function by engineering birefringence in a Mach-Zehnder interferometer (MZI), as schematically shown in Figure 2(a). The MZI is composed of two 2×2 directional couplers (DC) connected to two waveguide arms. The difference in refractive index between the waveguide core and cladding is 0.75%, and the birefringence for such 0.75%-Δ GeO_2 doped waveguide is on the order of 10^4 due to stress. The geometrical birefringence is negligible for the 6 μm × 6 μm symmetric core geometry used in the waveguide design. To create the desired birefringence [21], we introduce a waveguide section with a core dimension of 19 μm × 6 μm. Tapered waveguides are inserted between waveguides of

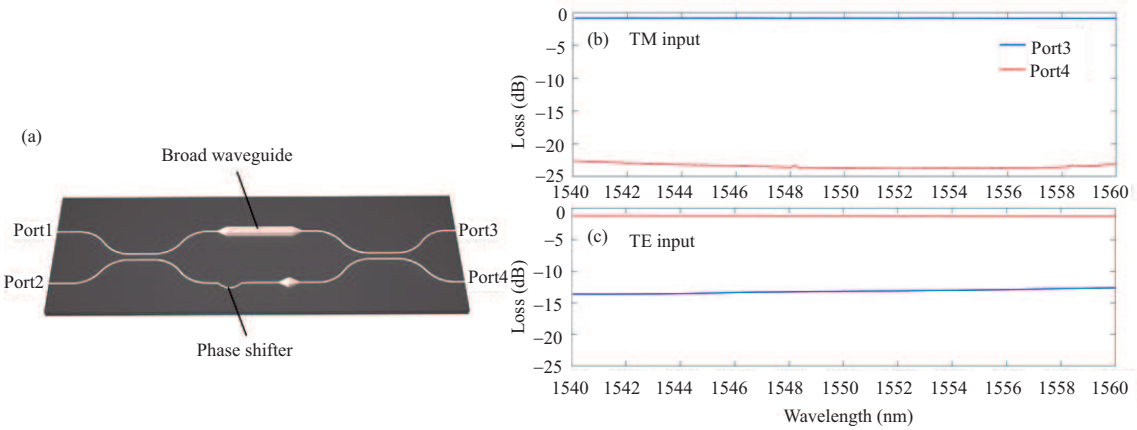

Figure 2 (Color online) (a) The schematic of silica-based PBS; (b) the transmittance spectra of the PBS for the through (Ports 1–3) paths; (c) the transmittance spectra of the PBS for the cross (Ports 1–4) paths.

varying widths to reduce excess loss, while identical tapered waveguides are inserted in another arm to balance optical path lengths and propagation losses. The length of the broad waveguide is meticulously selected to generate a π phase difference between TE and TM modes. An ΔL-long phase shifter section is added to one of the waveguide arms to ensure constructive (destructive) interference for the TE(TM) mode. With the above configuration, TM(TE) light entering Port 1 will primarily exit Port 3 (Port 4). The polarization extinction ratio (PER) of the PBS is determined by the length of the broad waveguide ($L_{\rm w}$), the length of the phase shifter (ΔL), and the DC splitting ratio (η). Assuming both DCs have a polarization-independent η, the output intensity of Ports 3 and 4 can be expressed as

$$\begin{aligned} I_3^{\rm TE(TM)} &= I_1^{\rm TE(TM)} \left[1 - 2\eta(1-\eta)\left(1+\cos\varphi_{12}^{\rm TE(TM)}\right)\right], \\ I_4^{\rm TE(TM)} &= I_1^{\rm TE(TM)} \left[2\eta(1-\eta)\left(1+\cos\varphi_{12}^{\rm TE(TM)}\right)\right], \end{aligned} \tag{1}$$

where the superscript TE(TM) denotes TE or TM modes, respectively, and φ_{12} denotes the phase difference between the two arms. To simultaneously achieve >20 dB PER for TE and TM, the following conditions must be met: $\eta = 0.50 \pm 0.04$, $\varphi_{12}^{\rm TE} = \pm 0.2$ rad, and $\varphi_{12}^{\rm TM} = \pi \pm 0.2$ rad. We note that design or fabrication discrepancies will have a greater impact on the performance of the TE mode because destruction interference at Port 3 is dependent on both η and φ_{12}.

We fabricated PBSs with different broad waveguide ($L_{\rm w}$) and phase shifter (ΔL) lengths on the same wafer. The best polarization splitting performance was observed in devices with $L_{\rm w} = 3650$ μm and $\Delta L = 0.18$ μm, as shown in Figures 2(b) and (c) by the transmittance spectra for through (Ports 1–3) and cross (Ports 1–4) paths. When TE(TM) light is emitted, the optical power is routed predominantly to the cross (through) path over the 1540–1560 nm spectral range, with a minimum PER of 13 dB (23 dB). The exceptional performance of TM mode suggests that the phase difference is precisely controlled. The relatively inferior TE performance is primarily attributable to the deviation from the ideal DC coupling ratio. The insertion loss is less than 1.5 dB, and wavelength dependence is negligible.

Being nominally polarization insensitive, silica-on-silicon platforms are unsuitable for on-chip PR techniques that typically rely on mode coupling. Although the necessary birefringence for PR can be externally induced by adding layers of heterogeneous materials [22] such as Si_3N_4 or polymer, it is easier to rotate polarization by inserting an ultrathin half-wave plate (HWP) into a silica-based waveguide. The HWP consists of a flexible polyimide film with low insertion loss, which can convert the TE to TM mode with high fidelity and vice versa. The HWP films were obtained from NTT Advanced Technology Corporation. The utilized HWP has a thickness and size of 15 μm and 0.75 mm $\times$ 0.5 mm, respectively. The groove in the waveguide was cut with a width and depth of 19 and 150 μm, respectively, by the blade of DISCO ZH05. In relation to the waveguide plane, the optical axis of the HWP was aligned at a 45° angle. The HWP was glued with the recommended UV-curing adhesive AT8224. The additional loss caused by the HWP was less than 1.0 dB. The measured PER of PR produced by the HWP exceeded 30 dB.

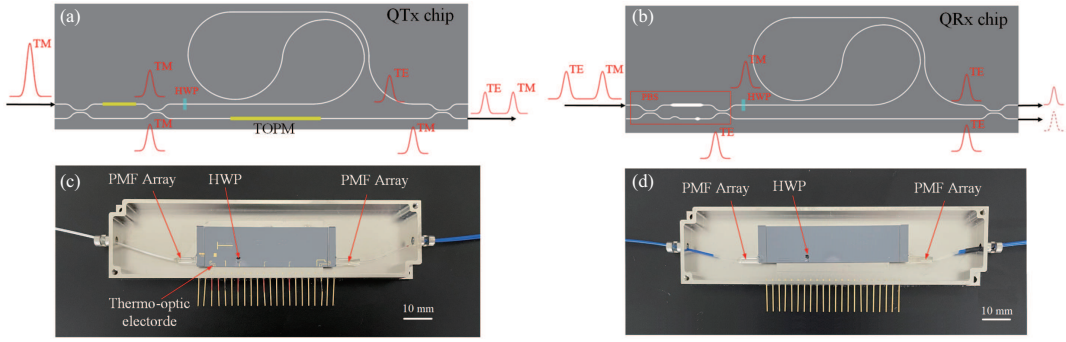

Figure 3 (Color online) (a) The structure diagram of QTx chip; (b) the photograph of the packaged QTx; (c) the structure diagram of QRx chip; (d) the photograph of the packaged QRx. Polarization maintaining fiber array (PMF array), Thermo-optic phase modulator (TOPM).

4 Quantum transmitter (QTx) and QRx

4.1 QTx and QRx chips

Figures 3(a) and (b) depict the structure diagram of the QTx chip and a photograph of the QTx module's internal packaging. The chip consists of an MZI serving as a tunable beam splitter, whose outputs are connected to the inputs of a DC via two waveguides of unequal lengths. Together, they form an AMZI with a 400 ps differential delay, which is suitable for 1.25 GHz QKD systems. In one arm of AMZI, the HWP was inserted into the waveguide to rotate the input pulse's polarization direction. The thermo-optical MZI divides a TM pulse into two parts as it enters the QTx. One pulse traverses the HWP, which rotates its polarization direction by 90°, and then the 400 ps delay line. The polarization direction remains unchanged as another pulse passes through the short arm of AMZI. The final output of QTx is a pair of pulses with orthogonal polarization direction and a 400 ps time interval. QTx chip dimensions are 56.1 mm × 16.2 mm. Gold wires connect the electrodes in the arms of MZI and the shorter arm of AMZI to the package. MZI's power-splitting ratio to AMZI is regulated by the electrodes in its arms. The electrodes in the shorter arm of AMZI are used to control the relative phase of the two pulses emitted by QTx. The measured fiber C fiber loss of the packaged QTx was 1.47 dB. The PER of QTx exceeds 20 dB.

In the QRx chip, we adopt an entirely passive design without the need for any electric adjustment. Figures 3(c) and (d) depict the structure diagram and photograph of the packaged QRx chip. It is an AMZI with a PBS entry. Similar to the QTx, an HWP was inserted into one arm of the AMZI. When the pulse pair with orthogonal polarization direction reaches QRx, PBS is utilized to route the two pulses deterministically. One of the pulses (first arrive) passes through the HWP and delay line, which rotates the polarization by 90°. Another pulse (last arrive) passes through AMZI's short arm. Then two pulses, which have the same polarization direction and temporally overlap, interfere on the coupler. As a result, the detector only detects a single-photon pulse. The size of the QRx chip is 61.2 mm × 14.8 mm. The measured fiber-fiber loss of the packaged QRx is 1.90 dB. When TM light is input into the chip, the PBS primarily directs the laser pulse to AMZI's long arm. The laser pulse is directed primarily to the short arm when initiating TE mode. In both instances, the measured PER is greater than 15 dB.

4.2 The interference visibility

We evaluate the suitability of QTx/QRx chips for QKD by measuring interference visibility. Imperfect interference visibility of $V < 1$ increases the quantum bit error rate (QBER) by a factor of $(1 - V)/2$ and decreases the system's SKR. Figure 4 depicts the evaluation configuration. The light source is a gain-switched semiconductor laser with a 50 ps pulse width and a 1546.6 nm central wavelength. A polarization controller is positioned between the QTx and QRx to calibrate the pulses' polarization. QTx and QRx are temperature regulated with a thermal C electrical cooler (TEC) to maintain phase stability.

According to Figure 4, the voltage applied to the thermo-optic electrode of MZI is V1, while the voltage applied to the short arm of AMZI is V2. To achieve optimal interference, we adjust the V1 voltage of QTx so that the power ratio of the double pulses output by QTx matches the loss ratio of the QRx's

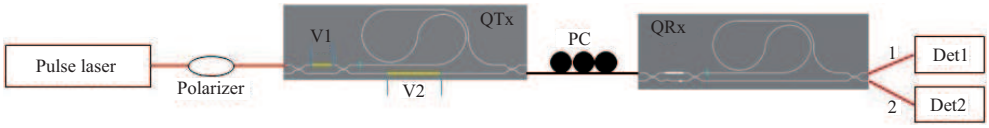

Figure 4 (Color online) The experimental setup to evaluate the visibility of the QTx and QRx. Red line: polarization maintaining fiber; black line: single-mode fiber.

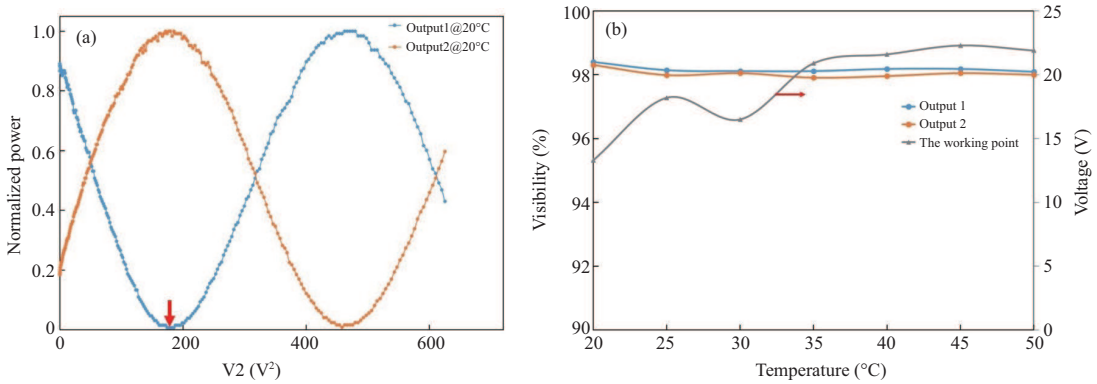

Figure 5 (Color online) (a) The interference fringes of output 1 and output 2 of QRx; (b) the visibilities and working points at different temperatures of TEC.

two arms. We determine the loss ratio of QRx's AMZI arms by simultaneously launching a pulsed laser with TE polarization from one of its output ports and measuring the corresponding power ratio of the double pulses with an oscilloscope. Due to the imperfection in the beam splitter of the QRx, two slightly different loss ratios will be obtained, and their average value will be used.

Figure 5(a) depicts the interference fringes measured for outputs 1 and 2 by varying the voltage V2 on the short arm of QTx to induce a thermal phase delay at 20°C. As shown in Figure 5(a), we obtain measurement visibilities of 98.4% and 98.3% for output 1 and output 2, respectively. When the interference pulse at output 1 becomes stronger, the pulse at output 2 becomes weaker, and vice versa. We attribute the imperfection in visibility to the output coupler's suboptimal splitting ratio. This imperfection contributes less than 1% to the QBER, which is acceptable for QKD applications. The AMZI devices can operate in a broad temperature range. Under varying device temperatures, interference fringes are nearly identical but horizontally displaced (not shown). Figure 5(b) shows that the average visibility remains greater than 98% throughout the tested temperature range. The secondary axis of Figure 5(b) illustrates the temperature dependence of the optimal working point for V2. In Figure 5(a), the red arrow indicates the working point at 20°C. This variation can be easily tracked in practical systems by a stabilization module employing QBER as the feedback signal.

5 Discussion

The first dual-polarization AMZI chips with on-chip PBS function for 1.25 GHz phase-encoding QKD systems have been fabricated. Due to fabrication process errors and the coupler splitting ratio, the PER of the PBS described in this paper is limited to 15 dB. In the dual-polarization phase-encoding QKD, imperfect polarization splitting will only introduce splitting loss and will not increase QBER. The 15 dB of PER corresponds to a polarization routing loss of 0.135 dB overall. As shown in Table 1, the measured QRx loss of 1.90 dB is superior to AMZIs based on other material platforms, such as Si_3N_4 [9] or silicon [12]. With the 3 dB polarization routing advantage, our QRx can support significantly higher SKRs in a QKD system with external, high-speed lithium niobate phase modulators for phase modulation. Based on the theoretical analysis of Lim2014 decoy-state protocol [23] and using practical InGaAs single-photon detectors with 30% efficiency and 2% after pulsing probability, and assuming the loss of commercial lithium niobate phase modulator is 2.5 dB, the SKR at transmission distance of 50 km is 1.47 Mbps, the 1.0% QBER induced by the imperfections of QTx and QRx would reduce SKR to 1.23 Mbps.

It should be noted that the chips in this paper are based on a refractive index difference of 0.75%.

Table 1 Comparison of chip-based QKD receiver interferometers

Platform	Delay (ps)	Power loss (dB)	Routing loss (dB)	Total loss (dB)	Dimension (mm^2)
Si_3N_4 [9]	500	4.5	3.01	7.51	4.0×8.0
Si [12]	960	15	3.01	18.01	3.2×5.1
SiO_2 [16]	400	3.31	3.01	6.32	27.8×23.1
This work	400	1.90	0.135	2.035	56.1×16.2

When a 2.0% refractive index difference is used, the dimensions of the chips can be greatly reduced, but the loss increases by approximately 1 dB. Existing QTx and QRx use different AMZI designs to optimize interference because the splitting ratio of DCs is highly sensitive to the waveguide dimension, resulting in low process tolerance. The development of an adiabatic coupler [24,25] was made possible by a structure with enhanced process tolerance. Improving the PER of the MZI-based PBS also necessitates better control of the coupler splitting ratio. With more precise couplers, the current QRx AMZI design also applies to the transmitter side. To achieve 99.9% interference visibility, the coupler splitting ratio must be within 0.50 ± 0.02.

6 Conclusion

In summary, we have developed the first dual-polarization AMZI chips capable of providing a 3-dB routing advantage for time-bin phase-encoding QKD. The power ratio of pulse pair for QTx could be adjustable which reduced the requirement of the coupler for QRx. The QRx is entirely passive and has a fiber-to-fiber loss of 1.90 dB. It was determined that the interference visibility of these chips exceeded 98.0% over a temperature range of 20°C–50°C. Our simulation demonstrates that these chips can support a secure rate of megabits per second over 50 km of fiber with these measured parameters. This work paves the way for a compact and practicable QKD module and encourages the expansion of QKD deployments.

References

1 Bennett C H, Bessette F, Brassard G, et al. Experimental quantum cryptography. J Cryptology, 1992, 5: 3–28
2 Yuan Z, Murakami A, Kujiraoka M, et al. 10-Mb/s quantum key distribution. J Lightwave Technol, 2018, 36: 3427–3433
3 Boaron A, Boso G, Rusca D, et al. Secure quantum key distribution over 421 km of optical fiber. Phys Rev Lett, 2018, 121: 190502
4 Lucamarini M, Yuan Z L, Dynes J F, et al. Overcoming the rate-distance limit of quantum key distribution without quantum repeaters. Nature, 2018, 557: 400–403
5 Wang S, Yin Z Q, He D Y, et al. Twin-field quantum key distribution over 830-km fibre. Nat Photon, 2022, 16: 154–161
6 Sibson P, Kennard J E, Stanisic S, et al. Integrated silicon photonics for high-speed quantum key distribution. Optica, 2017, 4: 172–177
7 Sibson P, Erven C, Godfrey M, et al. Chip-based quantum key distribution. Nat Commun, 2017, 8: 13984
8 Wang J, Sciarrino F, Laing A, et al. Integrated photonic quantum technologies. Nat Photon, 2020, 14: 273–284
9 Paraïso T K, Roger T, Marangon D G, et al. A photonic integrated quantum secure communication system. Nat Photon, 2021, 15: 850–856
10 Semenenko H, Sibson P, Hart A, et al. Chip-based measurement-device-independent quantum key distribution. Optica, 2020, 7: 238–242
11 Paraïso T K, De Marco I, Roger T, et al. A modulator-free quantum key distribution transmitter chip. npj Quantum Inf, 2019, 5: 42
12 Geng W, Zhang C, Zheng Y, et al. Stable quantum key distribution using a silicon photonic transceiver. Opt Express, 2019, 27: 29045–29054
13 Cao L, Luo W, Wang Y X, et al. Chip-based measurement-device-independent quantum key distribution using integrated silicon photonic systems. Phys Rev Appl, 2020, 14: 011001
14 Ren M, Li X, Zhang J, et al. Single-photon interference using silica-based AMZI with phase modulation. Opt Laser Tech, 2020, 122: 105837
15 Li X, Ren M, Zhang J, et al. Interference at the single-photon level based on silica photonics robust against channel disturbance. Photon Res, 2021, 9: 222–228
16 Zhang G W, Ding Y Y, Chen W, et al. Polarization-insensitive interferometer based on a hybrid integrated planar light-wave circuit. Photon Res, 2021, 9: 2176–2181
17 Marand C, Townsend P D. Quantum key distribution over distances as long as 30 km. Opt Lett, 1995, 20: 1695–1697
18 Martinez A, Fröhlich B, Dynes J F, et al. Quantum key distribution using in-line highly birefringent interferometers. Appl Phys Lett, 2018, 113: 031107

19 Xu H, Shi Y. Ultra-broadband silicon polarization splitter-rotator based on the multi-mode waveguide. Opt Express, 2017, 25: 18485–18491

20 Dai D, Wu H. Realization of a compact polarization splitter-rotator on silicon. Opt Lett, 2016, 41: 2346–2349

21 Hashizume Y, Goh T, Inoue Y, et al. Polarization beam splitter with different core widths and its application to dual-polarization optical hybrid. J Lightwave Technol, 2015, 33: 408–414

22 Samadian P, Hall T J. Performance analysis of polarization transformation waveguide structures for planar light circuits. Opt Quant Electron, 2016, 48: 96

23 Lim C C W, Curty M, Walenta N, et al. Concise security bounds for practical decoy-state quantum key distribution. Phys Rev A, 2014, 89: 022307

24 Deng X, Yan L, Jiang H, et al. Polarization-insensitive and broadband optical power splitter with a tunable power splitting ratio. IEEE Photon J, 2017, 9: 1–9

25 Wang Y, Gao S, Wang K, et al. Ultra-broadband and low-loss 3 dB optical power splitter based on adiabatic tapered silicon waveguides. Opt Lett, 2016, 41: 2053–2056